

## Research Paper

## Energy and materials analysis of wet channels structures for evaporative cooling systems manufactured by FFF technique with foam materials



Paula Conrat<sup>a,\*</sup>, Francisco Comino<sup>b</sup>, Jesús Castillo-González<sup>c</sup>, Francisco J. Navas-Martos<sup>c</sup>, Manuel Ruiz de Adana<sup>a</sup>

<sup>a</sup> Departamento de Química-Física y Termodinámica Aplicada, Escuela Politécnica Superior, Universidad de Córdoba, Campus de Rabanales, Antigua Carretera Nacional IV, km 396 14071, Córdoba, Spain

<sup>b</sup> Departamento de Mecánica, Escuela Politécnica Superior, Universidad de Córdoba, Campus de Rabanales, Antigua Carretera Nacional IV, km 396 14071, Córdoba, Spain

<sup>c</sup> Centro Tecnológico del Plástico Andaltec, Calle Vilches 34, Ampliación Polígono Cañada de la Fuente, 23600, Martos, Jaén, Spain

## ARTICLE INFO

## ABSTRACT

## Keywords:

Evaporative cooling  
Porous materials  
Wet channel  
Additive manufacturing  
Heat and mass Exchange

The development of new evaporative cooling technologies can significantly reduce energy consumption and help mitigate the effects of climate change. This study aimed to evaluate the evaporative cooling capacity of air passage channel structures. Six different channels were manufactured using two types of foam, Wfoam and Bfoam, three of each type, made from polylactic acid added with a chemical blowing agent, employing the Additive Manufacturing (AM) technique of fused filament fabrication and modifying manufacturing parameters. The experimental analysis consisted of two phases: initially, all six channels were tested under constant inlet air conditions; subsequently, the channel exhibiting the highest evaporative cooling capacity was further analysed under different air velocities. The results obtained allowed for an analysis of the relationship between material properties, energy performance, and cooling capacity, with the goal of optimizing and designing more efficient cooling systems. The energy performance of the channels was assessed in terms of heat flux, and sensible and latent powers. The results indicated that the channel made from the type of foam with the highest porosity achieved the lowest supply air temperature and the highest sensible and latent powers. Additionally, this channel demonstrated the highest wet bulb effectiveness, reaching up to 0.86 at the maximum tested air velocity. These findings confirm the feasibility of using AM to generate porosity in evaporative cooling systems manufactured with polymeric materials.

## 1. Introduction

The growing increase in energy demand, particularly in refrigeration systems, driven by demographic growth and industrialisation, poses significant challenges in terms of sustainability and resource depletion [1]. Specifically, the energy consumption of the Heating, Ventilation, and Air Conditioning (HVAC) systems constitutes approximately 45 % of building consumption [2]. This situation raises significant environmental concerns such as global warming, climate change, and greenhouse gas emissions [3], in particular HVAC systems, which produce 80 % of direct CO<sub>2</sub> emissions worldwide [2]. In view of the current situation, more efficient technologies, such as Evaporative Cooling (EC) systems, which utilise a heat and mass exchange process without a compressor and without refrigerants, are being developed [4].

There are two main types of EC systems: Direct Evaporative Cooling (DEC) systems, in which the outside air passes through a humid medium, typically porous, where water evaporates, resulting in an increase of the supply air humidity ratio and a reduction of the supply air temperature [5]. The second one, Indirect Evaporative Cooling (IEC) systems, employs the latent heat of water evaporation to lower the supply air temperature without adding humidity [6]. As shown in Fig. 1, the main difference is that IEC systems use two well-differentiated air streams that circulate through two different types of channels: (i) the wet channel, made of a porous material; and (ii) the dry channel, made of hydrophobic material. The porous material retains the necessary water to cool the secondary air stream that passes through the wet channel. This cooling effect is produced by the direct evaporation of the water available in the wet channel upon contact with air. The humid air stream generated in the wet channel, in turn, indirectly cools the primary air

\* Corresponding author.

E-mail address: [z12coesp@uco.es](mailto:z12coesp@uco.es) (P. Conrat).

<b>Nomenclature</b>			
$h$	Enthalpy [kJ/kg]	d	dew point
HF	heat flux [W/m <sup>2</sup> ]	e	accumulated evaporated water
$\dot{m}$	mass flow [kg/s]	i	inlet
$m$	mass [g]	l	latent
$m''$	mass per unit area [g/m <sup>2</sup> ]	max	maxim
P	pressure [Pa]	min	minim
PVA	pore volume of adsorption [cm <sup>3</sup> /g]	sa	supply air
PVD	pore volume of desorption [cm <sup>3</sup> /g]	s	sensible
$\dot{Q}$	power [kW]	w	water
Q	energy [kJ/m <sup>2</sup> ]	wall	channel wall
R	roughness [ $\mu\text{m}$ ]	wb	wet bulb
Rc	average of the peak-valley distances in a reference line [ $\mu\text{m}$ ]		
Rz	average of the maximum peak-valley distances in a reference line [ $\mu\text{m}$ ]		
S	primary surface [ $\mu\text{m}$ ]		
Sa	arithmetic mean height of the whole surface [ $\mu\text{m}$ ]		
SA	surface area [m <sup>2</sup> /g]		
Sq	mean squared of the height in the whole surface [ $\mu\text{m}$ ]		
t	time [min]		
T	temperature [°C]		
V	air velocity [m/s]		
<i>Greek letters</i>			
$\Delta$	differential		
$\varepsilon$	effectiveness [-]		
$\omega$	humidity ratio [kg/kg]		
$\sigma$	thermal conductivity [W/m·K]		
<i>Subscripts</i>			
aux	auxiliary		
		<i>Acronyms</i>	
		AC	air channel
		AHU	air handling unit
		AM	additive manufacturing
		CC	cooling coil
		CF	centrifugal fan
		CNC	computer numerical control
		DEC	direct evaporative cooling
		EC	evaporative cooling
		F	filter
		FC	flow conditioner
		FFF	fused filament fabrication
		HC	heating coil
		HVAC	heat ventilation air conditioning
		HX	heat exchanger
		IEC	indirect evaporative cooling
		PLA	polylactic acid
		SEM	scanning electron spectroscopy
		SH	steam humidifier
		TC	thermal camera

stream circulating through the dry channel, achieving efficient cooling without increasing the primary air stream's humidity ratio.

Typically, EC systems have been manufactured with metallic materials, such as copper, aluminium or steel, due to their hydrophobic properties [7]. Among these, aluminium is the most widely utilised owing to its excellent thermal conductivity, which in combination with other metals, porous ceramics, or fibrous hydrophilic materials, forms wet channels [8]. Recently, alternative materials were tested for dry channels, such as High-Density Polyethylene (HDPE) [9], Polylactic Acid (PLA) with bronze [10], Acrylonitrile Butadiene Styrene (ABS) [11], selected for their moisture resistance, durability, and low cost. For wet channels, materials such as felt [12], kraft [13], coconut [14], cellulose [15] and polymer-nickel foam [16] were selected due to their water absorption capacity, which is crucial for effective evaporative cooling. Some researchers have developed a biodegradable foaming filament from PLA to manufacture medical components with high porosity [17], which could be suitable for the fabrication of wet channels.

Conventional HVAC systems have traditionally been made of metallic materials and manufactured using Computer Numerical Control (CNC). However, due to the high production costs and limitations in manufacturing complex geometries, new techniques such as Additive Manufacturing (AM) are being explored for various applications. AM offers advantages in design versatility, weight reduction, and lower manufacturing costs [18]. Two identical prototypes of counterflow Heat Exchanger (HX), the first one composed of aluminium and the other of PLA, were manufactured using the Fused Filament Fabrication (FFF) technique, a type of AM. An analysis using a Scanning Electron Microscope (SEM) revealed that PLA exhibited a uniform and periodic

roughness, while the aluminium surface appeared disordered. Nonetheless, both materials demonstrated similar wetting conditions [19]. Sapienza et al. characterised a plastic HX and compared it with a metallic HX. The results showed that the plastic one delivered a cooling power of 2.40 kW/kg, whereas the metallic one achieved 2.34 kW/kg [20]. Notably, only one previous study was developed an IEC system using AM techniques with plastic materials. In this research, the prototype was manufactured as a single piece, with felt used as the porous material and PLA as the hydrophobic material, achieving dew-point effectiveness values up to 0.9 [10]. None of these studies investigated the effect of varying manufacturing parameters in AM on the production of a single wet channel using porous materials.

Several studies investigated the energetic performance of IEC systems. Velasco et al. experimentally compared two operation modes of a polycarbonate IEC, under dry and wet conditions at different air flow rates. Their results indicated that the prototype with water achieved a greater temperature variation and cooling capacity, particularly as the air volume flow decreased [21]. Another study compared an aluminium IEC with another with dry channels composed of PET and wet channels made of PET and cellulose, finding that both systems exhibited similar wet bulb effectiveness, ranging from 40–50 % [15]. Wang et al. developed ceramic foam to be used in both IEC and DEC system, measuring the dry bulb temperature and relative humidity of each system. Their analysis demonstrated that the cooling capacity increased gradually with the mass air flow [22].

Despite the growing research in AM technologies for various applications, the influence of manufacturing parameters on the development of foam materials for evaporative cooling systems has not been adequately explored. Additionally, there is a significant lack of studies

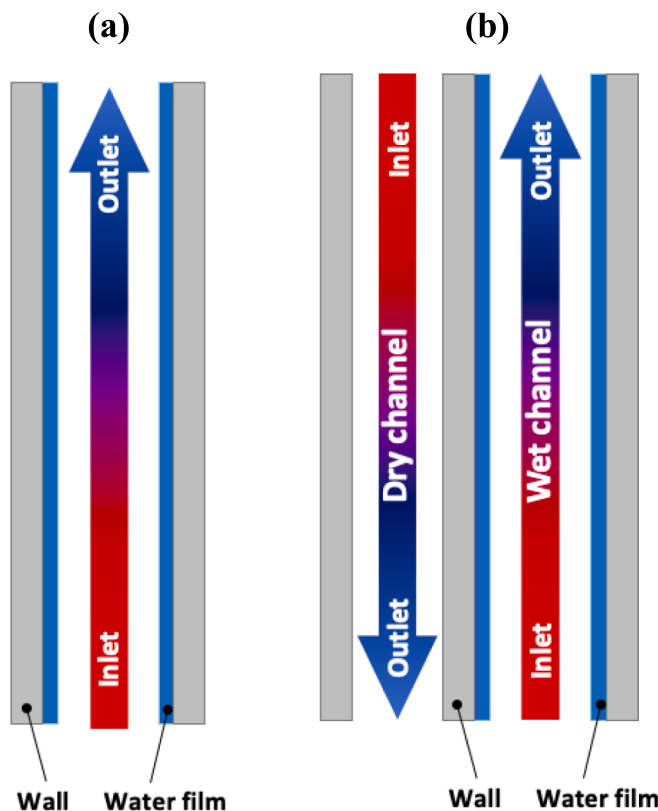


**Fig. 1.** Schematic diagram of (a) direct evaporative cooling and (b) indirect evaporative cooling.

on the fabrication and energy performance of wet channels made from different types of foam. AM technology offers considerable advantages, such as the ability to customize components according to specific requirements and the potential to use recycled materials, making it particularly attractive for these applications. The main objective of this work was to evaluate the cooling capacity of wet channels by varying the porosity. To achieve this, six wet channel structures were manufactured from two types of foam, adjusting the manufacturing parameters using the FFF technique.

## 2. Methodology

### 2.1. Manufacturing of foam materials

Two types of foam were selected in the present work: (a) Filaticum foam of white colour (Wfoam), supplied by Filamania KFT company (Hungary) and (b) BigRep foam of black colour (Bfoam), supplied by Bigrep GMBH company (Germany). Both types of foam were composed of PLA, which is the most widely used material in AM, due to its biodegradable characteristics and derived from organic origin [23]. Its rigidity and thermal stability under moderate conditions make it a suitable material for cooling system applications. A chemical blowing agent (CBA) was added to PLA to facilitate the creation of a porous structure. The resulting pores significantly increased the capacity of the material to absorb and retain water. Manufacturing parameters were also modified to generate macroporosity through AM: (a) Line width, space left between one bead and another, usually equal to the nozzle diameter, ranging from 0.4 mm to 0.8 mm; (b) Layer height, separation between layers, ranging from 0.2 mm to 0.3 mm; (c) Flow, percentage of material extruded compared to the theoretical amount that should be extruded, ranging from 50 % to 90 %; (d) Speed, velocity at which the print head moves, ranging from 40 mm/s to 80 mm/s. Three samples of Wfoam-based material configurations, from D1W to D3W, and another

three samples of Bfoam-based material configurations, from D1B to D3B, were manufactured. The manufacturing parameters of each foam material are shown in Table 1. An image of each foam material can be observed in Fig. 2. The 3D printer used was a Ultimaker 5S (UltiMaker, Netherland).

### 2.2. Characterization of foam materials

In order to analyse the different types of foam configurations, six samples were manufactured by FFF technique. The surface characteristics and thermal conductivity of each type of specimen were obtained.

#### 2.2.1. Surface analysis

The porosity was obtained through nitrogen adsorption and desorption isotherms. This test allowed to obtain surface area (SA), adsorption total pore volume (PVA) and desorption total pore volume (PVD) of a sample. A Micromeritics 3Flex Surface Characterization system (Canon, Japan) was used to carry out this analysis. In the present work, six cylindrical-shaped samples were manufactured, three Wfoam and three Bfoam, with a diameter of 8 mm and a height of 25 mm. The tests were conducted at 77 K for the six samples. These results made it possible to understand the relationship between the porosity of each material and the ability to retain a gas or liquid.

The microstructure of the different types of specimens was examined by scanning electron microscopy (SEM) using a JSM-7800F equipment (Jeol, Japan) to observe their morphologies, pore sizes, and microstructures. Six square samples of 9 mm sides were previously covered with a thin gold film, to make them conductive and suitable for SEM analysis.

The roughness and the primary surface of the samples were also examined by means of a confocal and interferometric microscope (DCM8, Leica, Spain) which had an equipment error of 3 %. Specifically, the following parameters were measured: (a) the sum of the maximum peak height and the maximum valley depth of a profile within the reference length,  $R_z$ ; (b) average of the peak-valley distances in a reference line,  $R_c$ ; (c) arithmetic mean height of the entire surface,  $S_a$ ; (d) mean square of the height in the entire surface,  $S_q$  and (e) maximum peak-valley distance in the entire surface,  $S_z$ .

#### 2.2.2. Thermal conductivity

The evaporative cooling units exchange both sensible and latent heat, so thermal conductivity ( $\sigma$ ) was measured for each type of foam. A heat flow meter (FOX50, Waters, England) was used to obtain  $\sigma$  values, with a conductivity range between 0.1 W/m K and 10 W/m K, with an accuracy of 3 %, according to ASTM C518. Cylindrical samples with a diameter of 55 mm and a thickness of 20 mm were manufactured to carry out the conductivity tests, as shown in Fig. 3.

### 2.3. Manufacturing of channel structures

Six different air passage channel structures were manufactured, one for each type of foam material configured previously. The channel structure was designed as a reference unit to compare the energy performance of each of the different material configurations considered. The envelope of the channel structure was composed of non-porous PLA and the interior of the channel structure of the different Bfoam-based and Wfoam-based materials, respectively. The structure has

**Table 1**  
Manufacturing parameters of foam materials.

Materials	D1W D1B	D2W D2B	D3W D3B
Line width [mm]	0.4	0.6	0.8
Layer height [mm]	0.2	0.3	0.3
Flow [%]	50	90	50
Speed [mm/s]	40	40	80

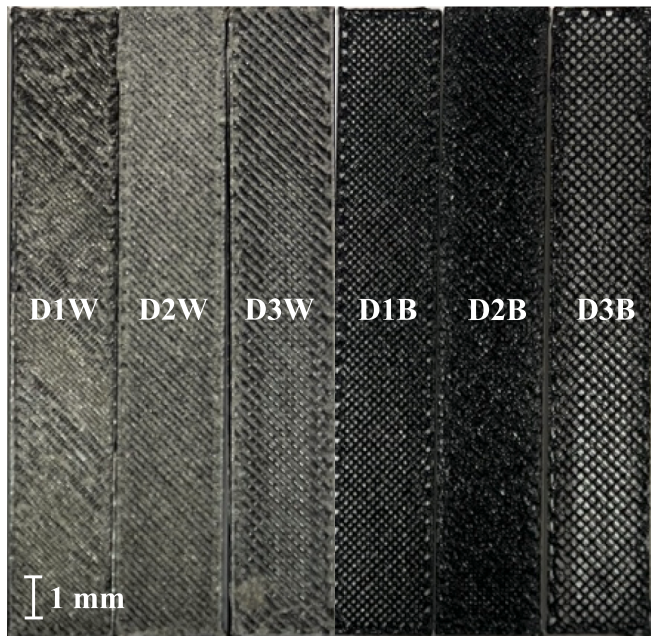


**Fig. 2.** Image of samples based on Wfoam and Bfoam.

dimensions of 310 mm long, 136 mm wide and 4.5 mm thick, it presents partition walls inside, resulting in a total free passage area of 322.5 mm<sup>2</sup> through which the air can circulate. A cross-sectional scheme and an image of one manufactured channel structure are shown in Fig. 4. The evaporative cooling potential of each channel structure was evaluated in order to determine its feasibility for use as an air treatment unit in a DEC system or as wet channel in an IEC system.

#### 2.4. Experimental setup

The channel structures previously manufactured were experimentally analysed in the HVAC laboratory of the University of Córdoba. The experimental setup was composed of an Air Handling Unit (AHU), a duct system and a monitoring system, see Fig. 5. The AHU was used to

generate the desired air inlet conditions, modifying air temperature, humidity ratio and air flow rate. The AHU had a cooling coil, a heating coil, a fan, a steam humidifier, and filters. The technical characteristics of experimental setup were included in a previous study [24].

The experimental setup consisted of several sensors with the purpose of analysing the energy behaviour of the channel structure: dry bulb temperature (T) sensors, dew point temperature ( $T_d$ ) sensors, heat flux (HF) sensors, and pressure difference ( $\Delta P$ ) sensors. A thermal camera (TC) was also used to obtain thermal images of the channel. The specific location and the technical features of each sensor are shown in Fig. 5 and Table 2, respectively.

#### 2.5. Experimental tests

The experimental test process consisted of immersing each channel structure in water for 30 min. Then, it was extracted and the water not absorbed by the foam material was removed. Finally, the channel structure was connected to the experimental setup, where the inlet air conditions were previously adjusted until they stabilized. In each experimental test, input and output variables were recorded at 3 s intervals for 30 min.

The experimental analysis of the channel structures was divided into two sets of tests: (i) the six channel structures were tested under constant inlet air conditions,  $T_i = 40^\circ\text{C}$ ,  $T_{d,i} = 10^\circ\text{C}$ ,  $V_i = 9.4 \text{ m/s}$ ; and (ii) the channel structures with the highest evaporative cooling capacity was analysed under different air velocities, 4.2 m/s, 9.4 m/s, 14.6 m/s, 19.8 m/s, in order to optimise its operation. The inlet air temperatures were also set constant,  $T_i = 40^\circ\text{C}$ ,  $T_{d,i} = 10^\circ\text{C}$ , for these tests.

#### 2.6. Heat transfer and effectiveness parameters

The following parameters were obtained for each experimental test to evaluate the energy behaviour of the channel structure:

- Sensible heat ( $\dot{Q}_s$ ) delivered by the channel structure was obtained with Eq. (1). It was calculated as the mass air flow rate ( $\dot{m}_{sa}$ ) multiplied by the difference between enthalpies of auxiliary and inlet air ( $h_{aux} - h_i$ ). The auxiliary state has the same dry bulb temperature as the inlet air and the same humidity ratio as the supply air.

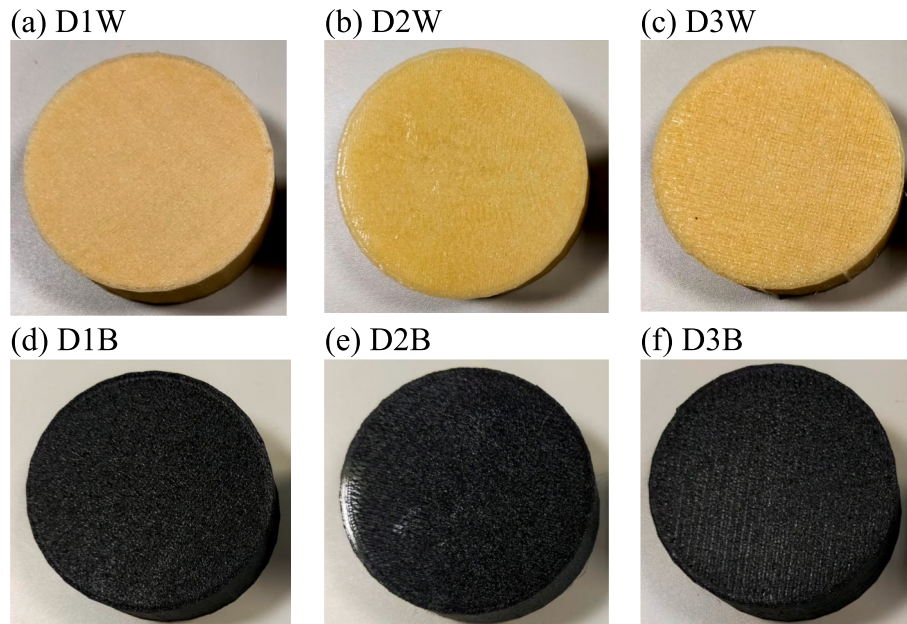


**Fig. 3.** Different types of samples for conductivity tests.

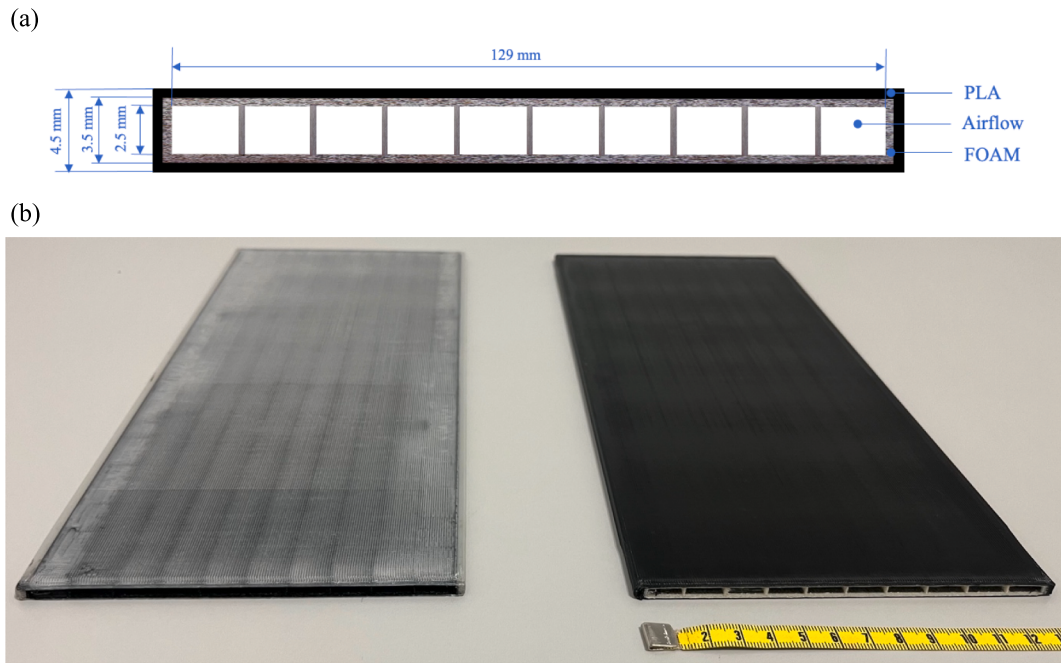


**Fig. 4.** (a) Cross section scheme (b) a real example of a manufactured channel structure.

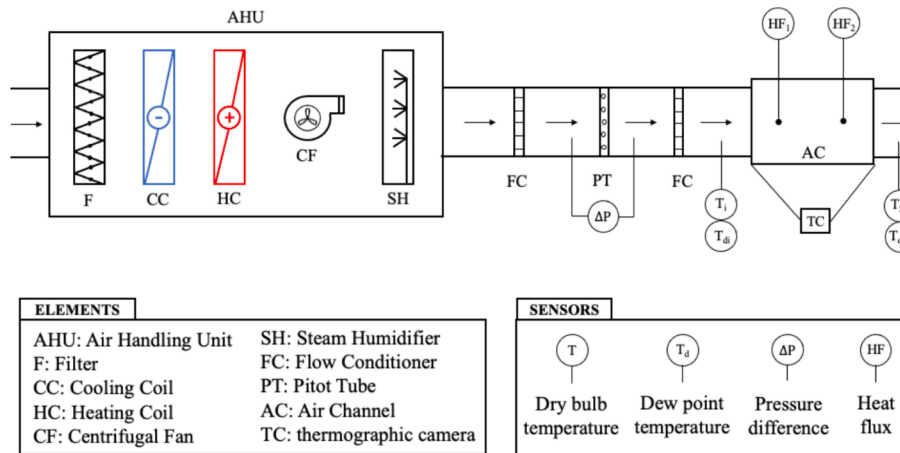


**Fig. 5.** Schematic of the experimental setup.

**Table 2**  
Technical specifications of the sensors.

Variable	Type of sensor	Manufacturer	Accuracy
T	Thermocouple type T	TC Medida y Control de Temperatura	$\pm 0.5^\circ\text{C}$
T <sub>d</sub>	Chilled mirror hygrometer	GE Measurement & Control Solutions	$\pm 0.15^\circ\text{C}$
HF	Heat Flux plate	Hukseflux Thermal Sensors	$\pm 3\%$
$\Delta P$	Differential pressure transmitter	Siemens	$\pm 5\%$
TC	Thermal camera	Flir One Pro	$\pm 3^\circ\text{C}$

$$\dot{Q}_s = \dot{m}_{sa} \cdot (h_{aux} - h_i) \quad (1)$$

- Latent heat ( $\dot{Q}_l$ ) delivered by the channel structure was obtained with Eq. (2). It was calculated as mass air flow rate ( $\dot{m}_{sa}$ ) multiplied by the difference between enthalpies of auxiliary and supply air ( $h_{sa} - h_{aux}$ ).

$$\dot{Q}_l = \dot{m}_{sa} \cdot (h_{sa} - h_{aux}) \quad (2)$$

- Mass of accumulated evaporated water in each channel structure ( $m_e$ ), according to Eq. (3). Where  $\dot{m}_{sa}$  is mass air flow rate and  $\Delta\omega$  is the difference in air humidity ratio between the inlet and supply air flow, integrated throughout the duration of the test.

$$m_e = \int_0^t \dot{m}_{sa} \cdot \Delta\omega \cdot dt \quad (3)$$

- Mass of accumulated evaporated water in each channel structure per unit area ( $m_e''$ ), according to Eq. (4). Where  $m_e$  divided by the area of the two walls of the channel ( $A_{wall}$ ).

$$m_e'' = \frac{m_e}{2 \cdot A_{wall}} \quad (4)$$

- Wet bulb effectiveness ( $\varepsilon_{wb}$ ) calculated as the ratio between the difference of inlet ( $T_i$ ) and supply ( $T_{sa}$ ) dry bulb temperatures and the difference between  $T_i$  and inlet wet bulb temperature ( $T_{wb,i}$ ), obtained with Eq. (5).

$$\varepsilon_{wb} = \frac{T_i - T_{sa}}{T_i - T_{wb,i}} \quad (5)$$

- Sensible thermal energy ( $Q_s$ ) per unit area of channel walls, delivered by the channel structure obtained with Eq. (6). Sensible thermal energy was calculated as the integral over the entire test time of the sensible heat, divided by the area of the two walls of the channel ( $A_{wall}$ ).

$$Q_s = \frac{1}{2 \cdot A_{wall}} \int \dot{Q}_s \cdot dt \quad (6)$$

- Latent thermal energy ( $Q_l$ ) per unit area of channel walls, delivered by the channel structure obtained with Eq. (7). Latent thermal energy was calculated as the integral over the entire test time of the latent heat, divided by the area of the two walls of the channel ( $A_{wall}$ ).

$$Q_l = \frac{1}{2 \cdot A_{wall}} \int \dot{Q}_l \cdot dt \quad (7)$$

### 3. Results and discussion

#### 3.1. Material analysis

The surface characteristics of the interior of the channel structure are of great importance since they allow the transfer of sensible and latent heat between the air and water flow. Therefore, the morphology, surface properties and conductivity of each manufactured foam material were analysed.

##### 3.1.1. Microstructure characterization

The porosity results are shown in Table 3. Wfoam-based samples exhibit higher values of SA, PVA and PVD than those Bfoam-based samples, which results in a higher porosity. Specifically, sample D1W presented the highest values, while sample D2B the lowest. This indicates that the variation in manufacturing parameters influences the porosity obtained in each sample.

The SEM analysis of the samples was carried out to observe their surface morphology. The SEM images obtained are shown in Fig. 6. The variation in the manufacturing parameters influenced the microstructure of the samples, as observed in the SEM images, which were taken with a magnification of 40x, to obtain a detailed visualization of the surface morphology and structural features.

It can be seen that the D1 samples of both types of foam were fibrous with elongated pores, the filaments were also the narrowest compared to the other samples and even some were connected and others broken (see Fig. 6a and Fig. 6d). This was due to having the smallest line width value (0.4 mm), which is the same as the diameter of the nozzle, and a flow value of 50 % for the material being extruded. However, the microporosity generated within the filaments was due to the chemical blowing agent and the macroporosity was generated by the manufacturing parameters. For D2W and D2B, solid areas with attached filaments were generated, there wasn't separation between threads, mainly due to flow

value of 90 % which was the highest (see Fig. 6b and Fig. 6e). An irregular surface was also generated. These samples exhibited the lowest porosity, as shown in Table 3. Well-defined and homogeneous filaments are shown in Fig. 6c and Fig. 6f, corresponding to samples D3W and D3B respectively, which had the highest line width (0.8 mm).

#### 3.1.2. Analysis of roughness and primary surface

The results of roughness and primary surface measurement for each sample are shown in Table 4. Also, the 3D topography of Sz was performed for each sample, see Fig. 7, where peaks and valleys were observed in the entire surface. It can be seen that the highest Roughness (R) and Primary Surface (S) values of the Wfoam-based specimens were achieved by D1W, followed by D3W, and finally D2W, and for the Bfoam-based specimens, the highest values were achieved by D3B, D1B and finally D2B. This trend was the same as that of porosity, as shown in Table 3. R and S values for D2W and D2B are the lowest due to the flow values (see Table 1). These results also agree with those observed in the SEM images, see Fig. 6.

#### 3.1.3. Analysis of the thermal conductivity

For this study, two thermal conductivity tests were conducted on each sample. The results for the two tests and their average value are shown in Table 5. The highest  $\sigma$  value of the Wfoam-based specimens was D3W, followed by D1W, and finally D2W, and for the Bfoam-based specimens, the highest value was found in D1B, followed by D3B, and finally D2B. However, these results were very close in all cases, so it cannot be concluded that the changes made in the AM parameters significantly modify the thermal conductivity of the samples.

#### 3.2. Energy analysis

Six experimental tests were conducted to analyse the energy behaviour of six channel structures manufactured with foam material configurations. Initially, all the channel structures were evaluated under a specific flow rate (9.4 m/s), and then, the structure exhibiting the highest cooling capacity was further analysed under four different air flow rates (4.2 m/s, 9.4 m/s, 14.6 m/s, 19.8 m/s).

##### 3.2.1. Analysis of the channel structure at specific air flow rate

The supply air conditions of the six channels are presented in Fig. 8. During the dynamic test of each channel, different phases can be observed. In Fig. 8a, the supply air dry bulb temperatures ( $T_{sa}$ ) began to reduce gradually until reaching a minimum value (phase 1). This decline occurred because the water present in the channels began to evaporate. Evaporation is an energy-demanding process, and this energy is removed from the system in the form of heat, causing a decrease in temperature. After reaching their minimum values,  $T_{sa}$  began to increase (phase 2), indicating the loss of evaporative cooling capacity due to the depletion of water inside the channels. Finally, when the channels were dry,  $T_{sa}$  values increased slightly (phase 3). In last phase, the  $T_{sa}$  values were not equal to the inlet air temperature due to sensible heat transfer between the channel walls and the outside conditions. It is expected that given a longer period of time, both temperature values will become equal.

The duration of phase 1, that is, where the evaporative cooling effect was maximum, depended on the type of channel tested. For example, channel D1W managed to reduce  $T_{sa}$  for 20 min, reaching a minimum value of 25.75 °C. However, channel D2W reduced  $T_{sa}$  for 2.15 min, reaching a minimum value of 27.52 °C. For both types of foam (Wfoam and Bfoam), the minimum  $T_{sa}$  values were obtained for channels D1W and D1B. These materials configurations exhibited the highest porosity and roughness, as shown in Table 3 and Table 4. Therefore, the surface properties of these materials influenced the cooling capacity of the channels.

In Fig. 8b, it can be observed that the supply air dew point temperature ( $T_{d,sa}$ ) values initially increased in all cases, due to the

**Table 3**  
Results of porosity of the six samples.

Materials	D1W	D2W	D3W	D1B	D2B	D3B
SA [m <sup>2</sup> /g]	1.17	0.54	0.86	0.81	0.42	0.8
PVA [cm <sup>3</sup> /g]	0.0008	0.0004	0.0007	0.0006	0.0003	0.0005
PVD (x10 <sup>5</sup> ) [cm <sup>3</sup> /g]	22	12	15	14	6	13

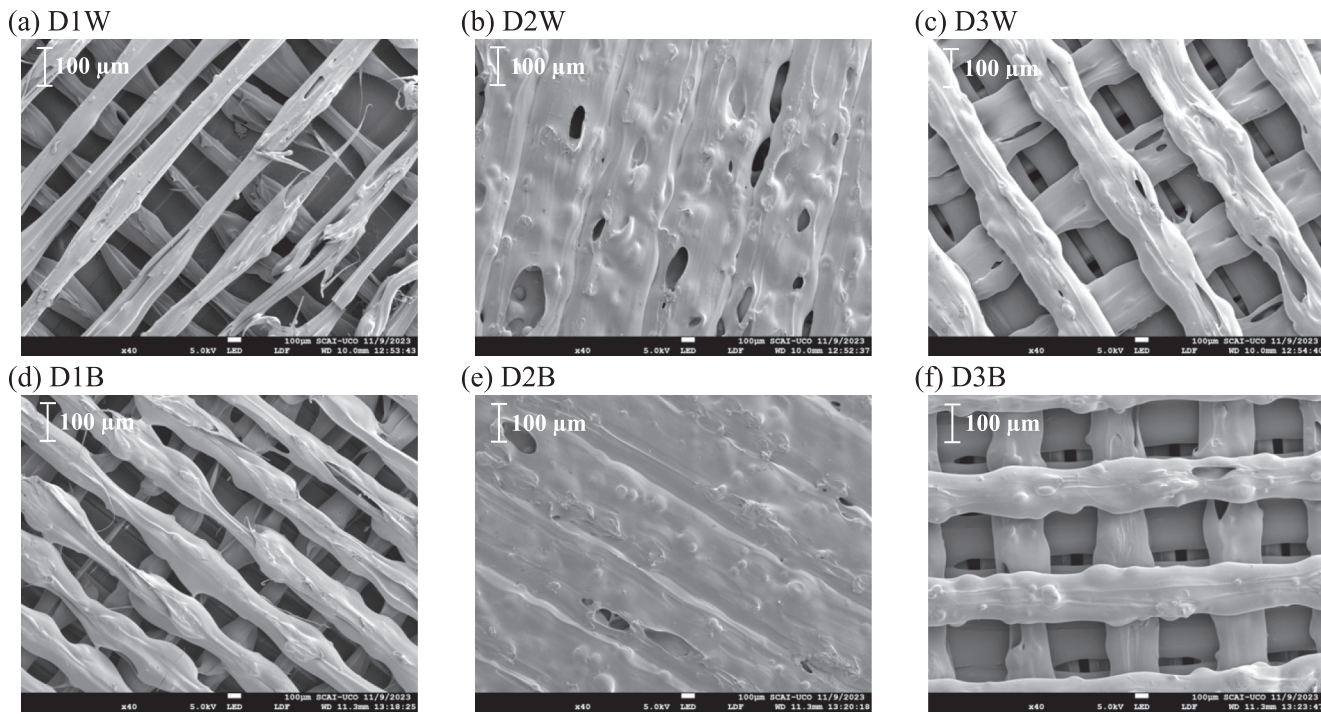


**Fig. 6.** SEM images of the surface of the samples.

**Table 4**  
Results of roughness and primary surface of the six samples.

Materials	D1W	D2W	D3W	D1B	D2B	D3B
Rz [μm]	328.31 ± 9.85	36.09 ± 1.08	164.75 ± 4.94	140.44 ± 4.21	52.23 ± 1.57	219.73 ± 6.59
Rc [μm]	238.43 ± 7.15	19.42 ± 0.58	114.04 ± 3.42	117.39 ± 3.52	46.21 ± 1.38	151.92 ± 4.55
Sa [μm]	70.87 ± 2.13	12.56 ± 0.38	46.34 ± 1.39	56.44 ± 1.69	7.29 ± 0.22	69.24 ± 2.07
Sq [μm]	92.77 ± 2.78	20.45 ± 0.61	64.79 ± 1.94	78.1 ± 2.34	12.83 ± 0.38	85.81 ± 2.57

humidification of the air stream, and then,  $T_{d,sa}$  decreased due to the loss of water within the channel. The  $T_{d,sa}$  values were equal to inlet dew point temperature when the channels were dry, that is, from this moment on, no water evaporation occurred.

For channel D1W, the  $T_{d,sa}$  values remained almost constant (approximately 21.5 °C) for 20 min. These results coincided with phases 1 of  $T_{sa}$ , see Fig. 8a. For the same channel, at the end of the test,  $T_{d,sa}$  did not reach the inlet dew point temperature value (10° C), because it was still wet. On the other hand, channel D2B (the sample with the lowest porosity and roughness),  $T_{d,sa}$  achieved the inlet dew point temperature after 10 min of testing, resulting in a rapid increase in  $T_{sa}$  value (see Fig. 8a). Therefore, the porosity and roughness properties of the channel significantly affected the supply air conditions.

The sensible and latent heat for each channel structure were calculated (see Fig. 9). The sensible power is related to the cooling capacity and the latent power to the ability of the air to evaporate water. The maximum sensible heat was 51 W achieved with the D1W type. On the other hand, the latent heat values were positive during the evaporative process. The sensible and latent heat results followed the same trends as  $T_{sa}$  and  $T_{d,sa}$  values, respectively, see Fig. 8.

Two heat flow (HF) sensors were placed on the channel walls, see Fig. 5, to measure the HF transfer between the environment (constant at 24 °C) and the interior of the channel. The HF data recorded for each test are shown in Fig. 10. It can be observed that initially the HF values were the highest, since the direction of HF was from the environment to the

interior of the channel (endothermic process), absorbing heat due to the evaporative cooling effect. Then, the HF values decreased as the evaporative cooling effect was reduced,  $T_{sa}$  increased and  $T_{d,sa}$  decreased, see Fig. 8. The HF values became negative when the material lost its evaporative cooling capacity, that is, it was dry. The direction of HF went from the interior of the channel towards the environment (exothermic process). In all cases, the HF1 sensor reached negative values before that the HF2 sensor, due to its location. That is, the foam material where HF1 was located was dried before the material where HF2 was located, following the direction of the air flow.

The HF2 values of channel D1W did not reach negative values throughout the test, see Fig. 10a, which denotes that the channel did not dry out at the end and the evaporative cooling effect continued. On the other hand, channel D2B structure lost its evaporative cooling capacity during the first 10 min, therefore, the HF values ended up being negative.

The mass of accumulated evaporated water in each channel per unit area ( $m_e''$ ) is an important parameter to evaluate the water retention capacity of each type of channel structure and the mass transfer process between water and the air stream.  $m_e''$  results are shown in Fig. 11. The channel structure that generated the highest  $m_e''$  was D1W type, followed by D1B, D3B, D3W, D2W and finally D2B. The difference in the evaporation rate could be due to the surface roughness, which determines the surface evaporation resistance. Through the images obtained from the SEM (Fig. 6) it was observed that samples D2W and D2B had no separation between threads and the lowest porosity (Table 3), which explains why they retained the least amount of water, resulting in the lowest  $m_e''$  values.

The evaporation process of the channels can be divided into two stages. The first stage occurred during a significant mass transfer between water vapor and the air stream. This stage is represented with a linear trend in all cases. Therefore, the greater the slope of the accumulated evaporated water curve, the greater the evaporation rate. The second stage was when it reached a constant accumulated evaporation rate, the maximum water retention capacity. During this stage, the channel structure stopped evaporating water into the airstream, thereby ending the evaporative cooling process ended. Previous research works

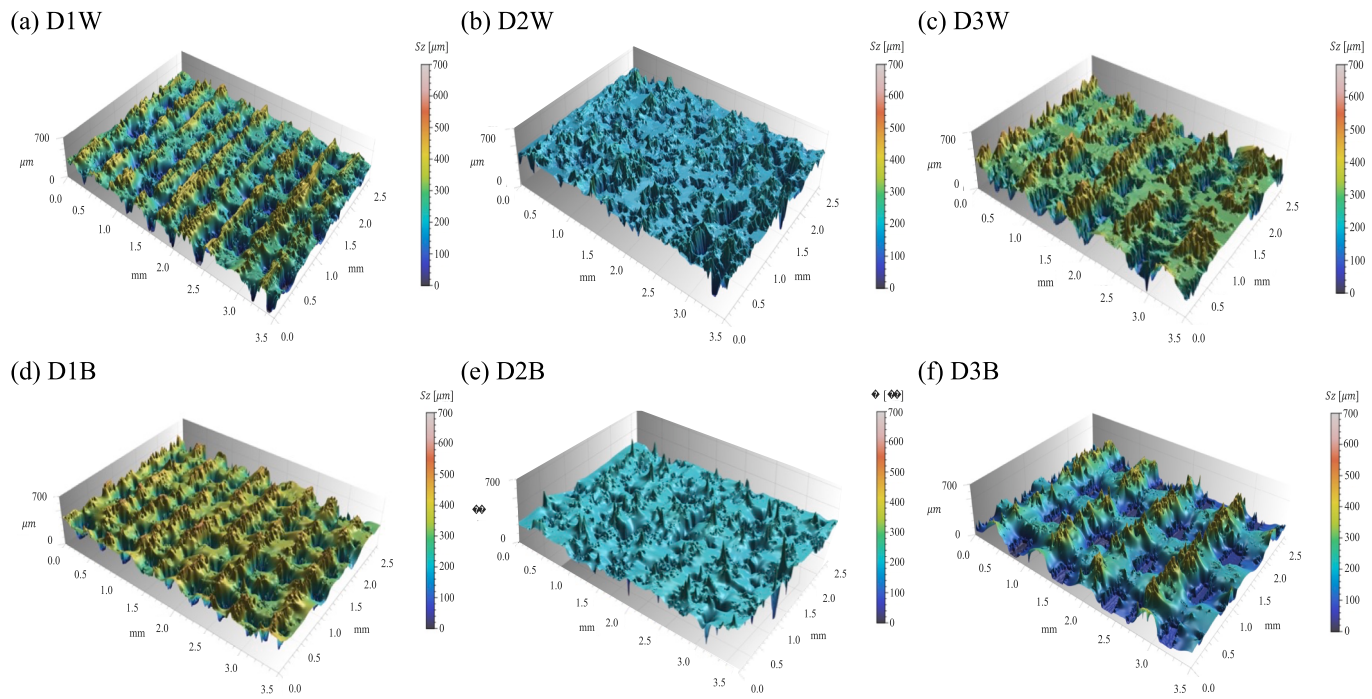


**Fig. 7.** Primary surface profiles ( $Sz$ ) measured by confocal microscope.

**Table 5**

Thermal conductivity results of the samples.

Materials	D1W	D2W	D3W	D1B	D2B	D3B
$\sigma$ [W/m·K]	$0.0976 \pm 0.0029$	$0.0972 \pm 0.0029$	$0.1020 \pm 0.0029$	$0.1160 \pm 0.0031$	$0.1120 \pm 0.0034$	$0.1130 \pm 0.0034$
Test 1	$0.0972 \pm 0.0029$	$0.0948 \pm 0.0028$	$0.1020 \pm 0.0029$	$0.1170 \pm 0.0031$	$0.1130 \pm 0.0034$	$0.1130 \pm 0.0034$
Average	$0.0974 \pm 0.0003$	$0.0946 \pm 0.0017$	$0.1020 \pm 0$	$0.1165 \pm 0.0007$	$0.1125 \pm 0.0007$	$0.1130 \pm 0$

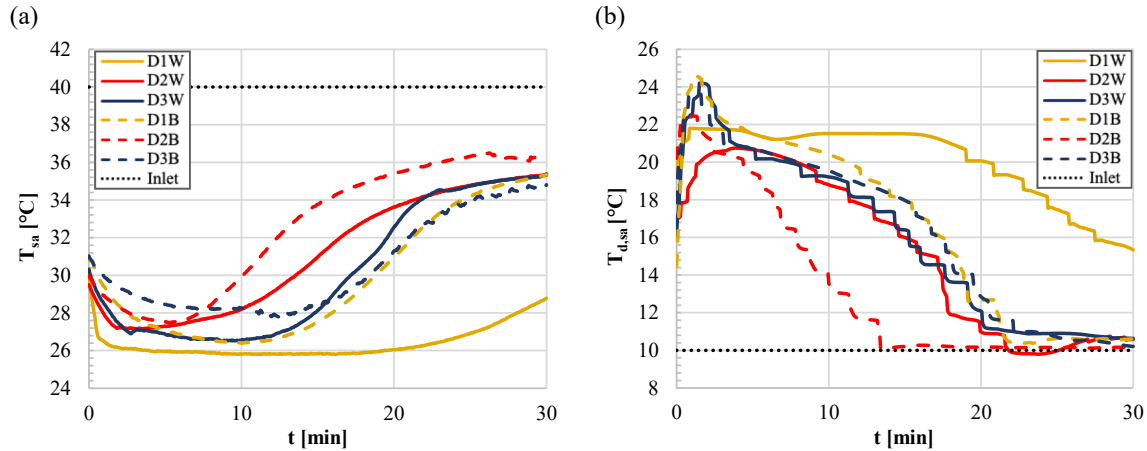


**Fig. 8.** Evolution of (a) supply air dry bulb temperature ( $T_{sa}$ ) and (b) supply air dew point temperature ( $T_{d,sa}$ ) over test time, for the six channels.

also analysed the mass of accumulated evaporated water in an evaporative cooling system, showing a similar two stage pattern [25–26].

In this study, the slopes were similar in all the channels. Thus, the main difference in terms of evaporative cooling was the amount of water accumulated in each type. The results show that the channel with the highest mass of accumulated evaporated water, which was  $170 \text{ g/m}^2$ , and the greatest evaporative cooling effect was the D1W.

In order to select the channel with the highest evaporative cooling effect, a radial graph with the most representative parameters

previously obtained for the six samples was represented in Fig. 12. The quantitative properties analysed were porosity, roughness, minimum air supply temperature and mass of accumulated evaporated water. The number 1 represents the channel that performed best for each property and 6 the worst. The results obtained from SEM were qualitative, and the thermal conductivity results were inconclusive, therefore they were not included in the radial graph.

The sample with the best score was D1W, excelling in all four properties studied, the highest values of porosity and roughness, the

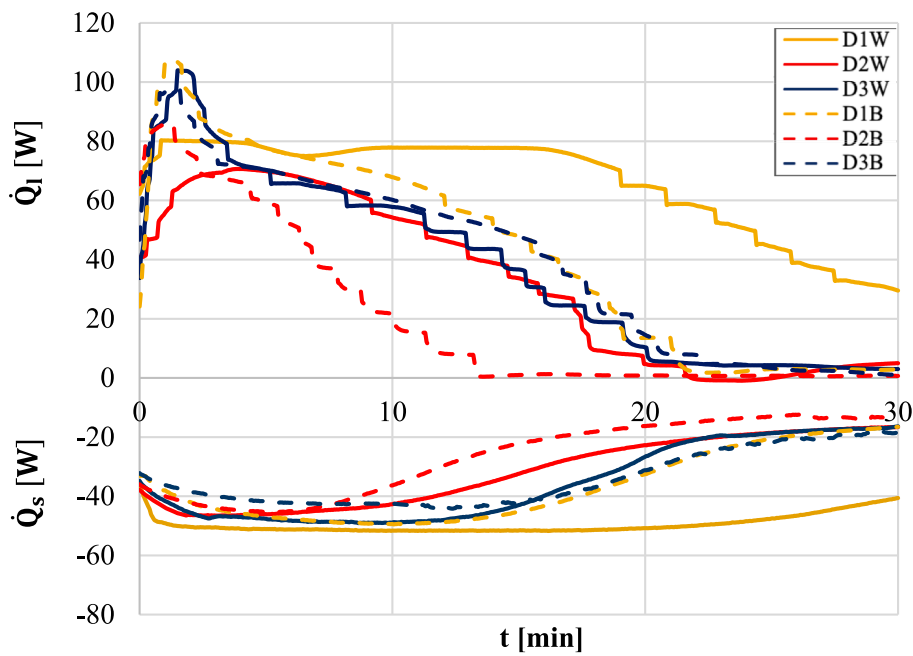


**Fig. 9.** Evolution of latent and sensible heat over test time for the six channels.

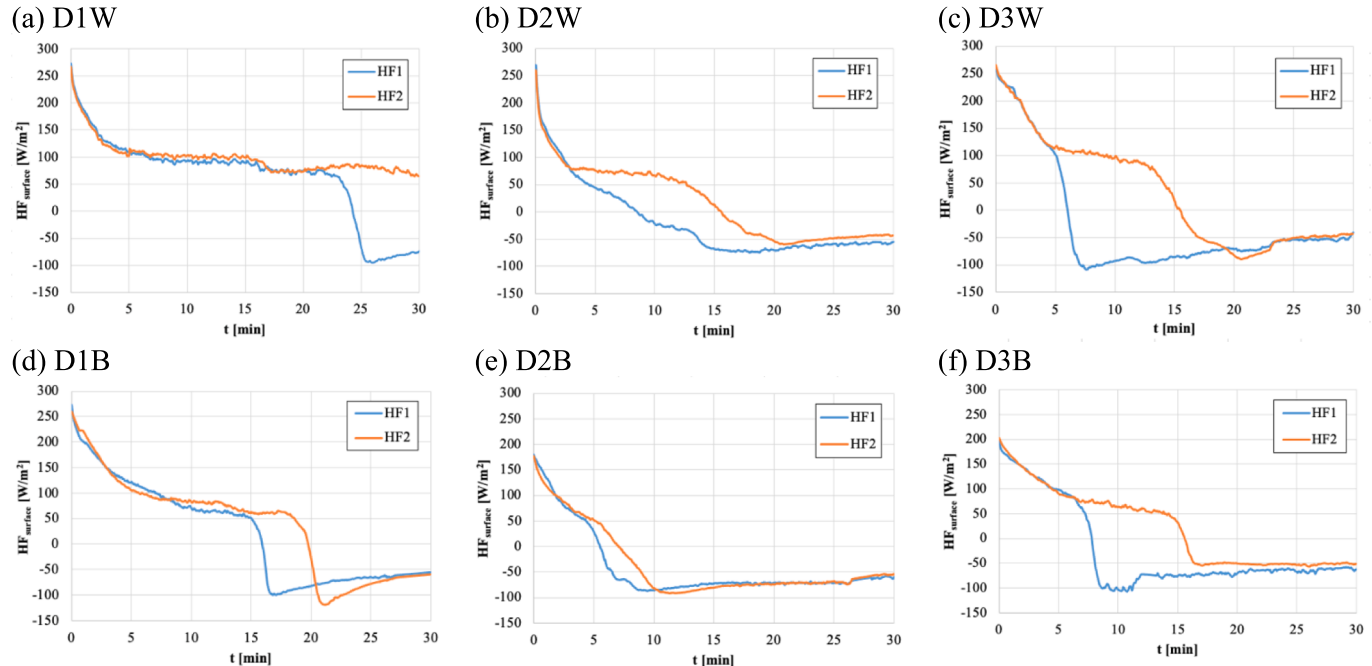


**Fig. 10.** Evolution of heat flow over test time for the six channels.

lowest supply air temperature resulting in the highest cooling power, and the greatest accumulated evaporated water, which is related to the evaporative cooling capacity. This was followed by D1B, D3W, D3B, D2W, D2B. Which means that the manufacturing parameters of the D1W and D1B sample were optimal (line width 0.4 mm, layer height 0.2 mm, flow 50 % and speed 40 mm/s) and in all cases the Wfoam-based was better than Bfoam-based material.

### 3.2.2. Analysis of operational parameters

As the channel D1W obtained the best properties, it was analysed at four different air velocities (4.2 m/s, 9.4 m/s, 14.6 m/s, 19.8 m/s), in order to optimise its operation. Dry bulb temperature ( $T_{d,sa}$ ), dew point

temperature ( $T_{d,sa}$ ), heat fluxes (HF), and sensible and latent heat ( $\dot{Q}_s$  and  $\dot{Q}_l$ ) were measured for each case study, as shown in Fig. 13. Thermographic images every 5 min were also obtained to analyse the evolution of channel surface temperatures and water evaporation.

$T_{sa}$  started with minimum values and subsequently increases, while  $T_{d,sa}$  initially had the highest values and then decreases. This occurred because the channel lost retained water and cooling capacity. Sensible heat was related to the cooling capacity and followed the same trend as  $T_{sa}$ , and latent heat was related to the humidity ratio and follows the trend of  $T_{d,sa}$ . In both cases,  $\dot{Q}_s$  and  $\dot{Q}_l$  increased in absolute value with velocity, this trend was coherent with the results obtained by the authors in previous research works [27].

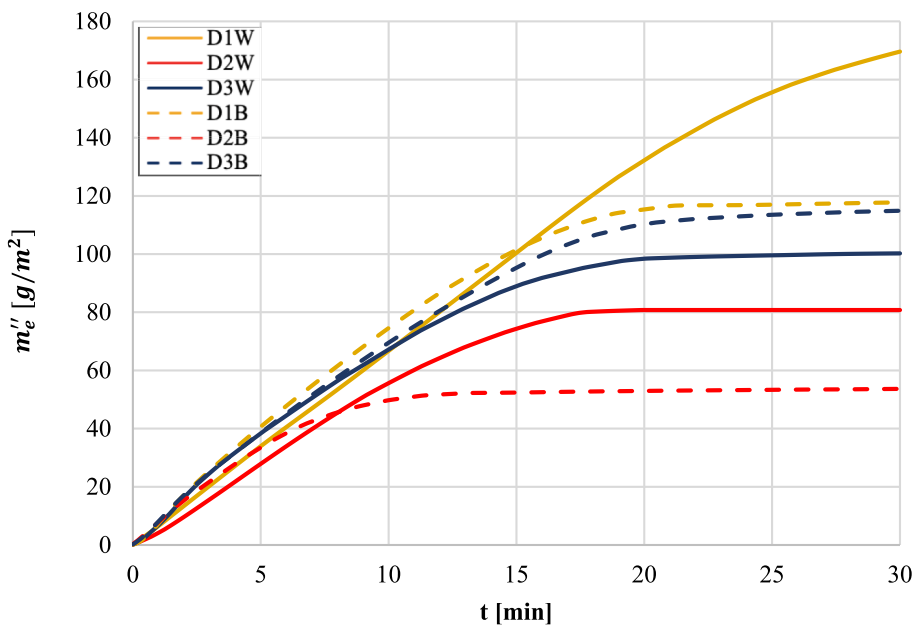


Fig. 11. Results of accumulated mass of evaporated water in each channel per unit area for the six channels.

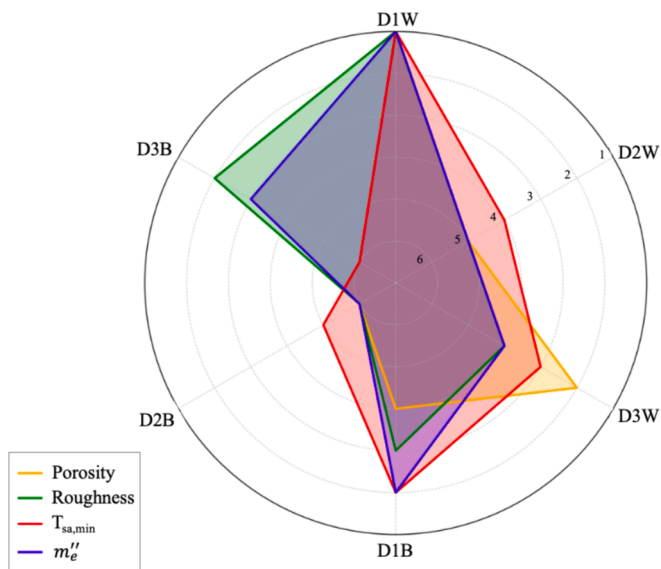


Fig. 12. Radial graph of the properties of the six samples with the scores.

For the heat flow, initially, HF1 and HF2 had the highest value, which decreased over time. In all cases, HF1 decreased before HF2, which was the sensor closest to the air inlet. In Fig. 13a and Fig. 13b the channel didn't manage to dry completely, as observed in the thermal camera images, specifically showing a darker area corresponding to water in the last image. As the inlet air flow rate increased, it was observed that the drying of the channel occurs sooner. Analysing Fig. 13c more specifically, all the lines become constant at minute 21 because the channel lost its water from inside, and thus, the evaporative effect capacity. The thermal camera image taken at this moment showed that the channel was completely dry.

The results of sensible and latent energy per unit area for channel D1W at four air velocities are presented in Fig. 14. For each case study, the minimum supply air temperature and the maximum wet bulb effectiveness are also shown. The energy trends were similar to those observed for sensible and latent heat: higher air velocities were associated with increased sensible and latent energy, being  $-1931.03 \text{ kJ/m}^2$

and  $1558.62 \text{ kJ/m}^2$  respectively. As the air velocities increased,  $T_{sa,min}$  decreased, indicating an increase in evaporative cooling capacity. However, a slight temperature reduction was obtained at high velocities, from  $14.6 \text{ m/s}$  to  $19.8 \text{ m/s}$ , with a consistent reduction of  $23.6^\circ\text{C}$  for both cases. Therefore, these results suggest that a minimum temperature limit was reached. These values were also in accordance with wet bulb effectiveness ( $\varepsilon_{wb,max}$ ), with a maximum value of 0.86 for  $19.8 \text{ m/s}$ . In previous work on evaporative cooling systems, an IEC made of PET with cellulose was manufactured. The wet bulb effectiveness of the composite IEC was obtained, ranging from 0.38 to 0.51. This was compared to an aluminum IEC, which exhibited a wet bulb effectiveness ranging from 0.40 to 0.47 [15]. Therefore, the manufactured wet channel achieved higher  $\varepsilon_{wb,max}$  values compared to previously studied systems.

#### 4. Conclusions

In the present study, the influence of manufacturing parameters and operating conditions on the evaporative cooling capacity of two types of foam (Wfoam and Bfoam) was investigated. Six wet channel structures were fabricated using additive manufacturing with the Fused Filament Fabrication technique. The key findings of this study are as follows:

- The analysis of material properties showed that the Wfoam-based material achieved greater porosity compared to the Bfoam-based material. Roughness and primary surface measurements followed the same trend as porosity, with the Wfoam-based material, particularly the D1W sample, achieving the highest values. SEM analysis allowed for the observation of how variations in the manufacturing parameters influenced the morphology of the samples.
- The experimental results showed that the channel D1W achieved the highest mass of accumulated evaporated water, maintaining the evaporative cooling effect for longer periods than the other channels. It reaching the lowest supply air temperature ( $25.75^\circ\text{C}$ ) of all the channels. Given the relationship between temperature and cooling power, the channel D1W exhibited the highest sensible heat.
- Empirical results for the channel D1W at different air velocities showed that as the airflow increased, the supply air temperature decreased. Consequently, both sensible and latent capacity and energy increased. For the highest air velocities examined, the minimum supply air temperature remained constant, suggesting the existence

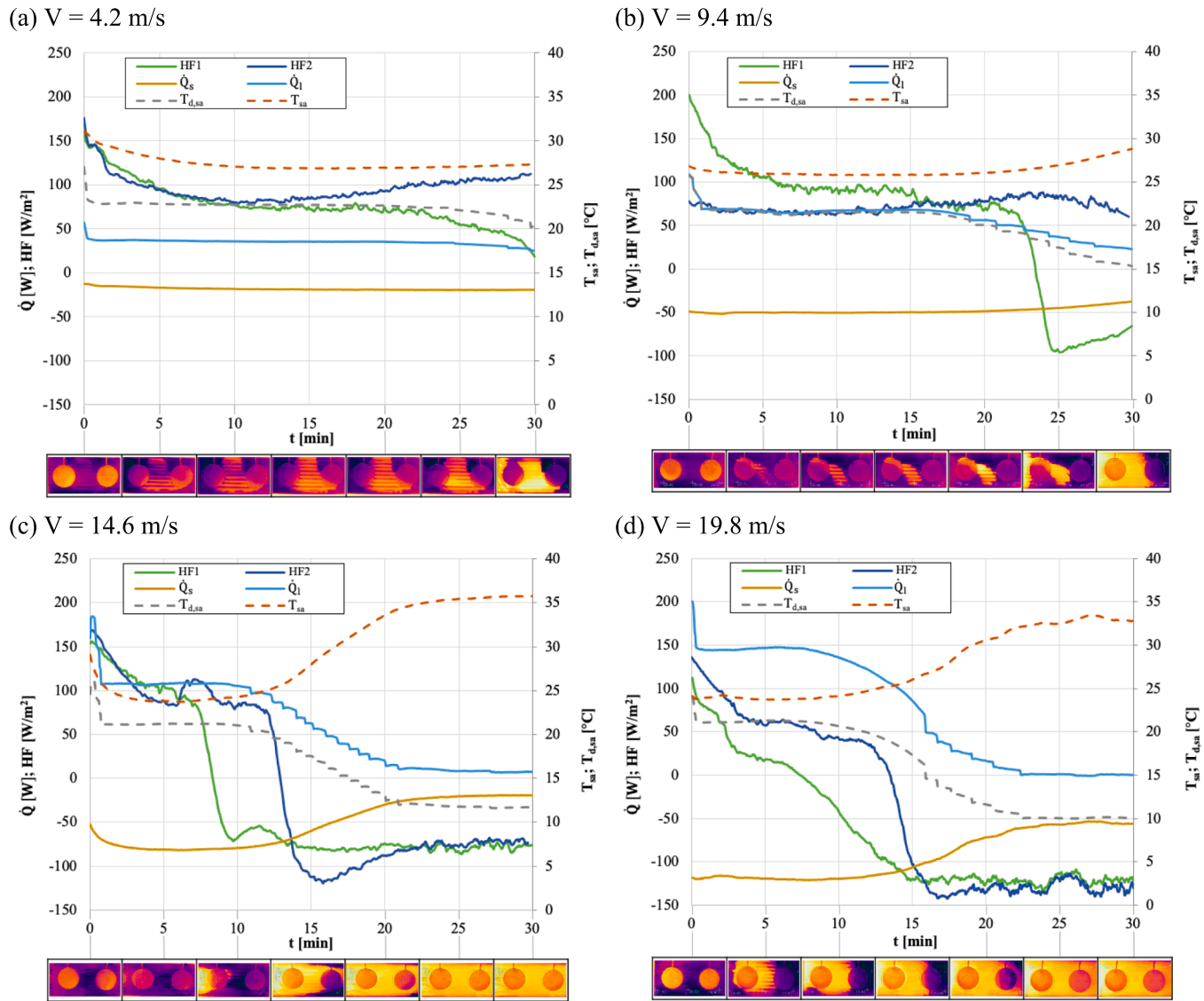


**Fig. 13.** Overlay of sensible and latent heat, temperatures and heat flow graphs of D1W type channel.

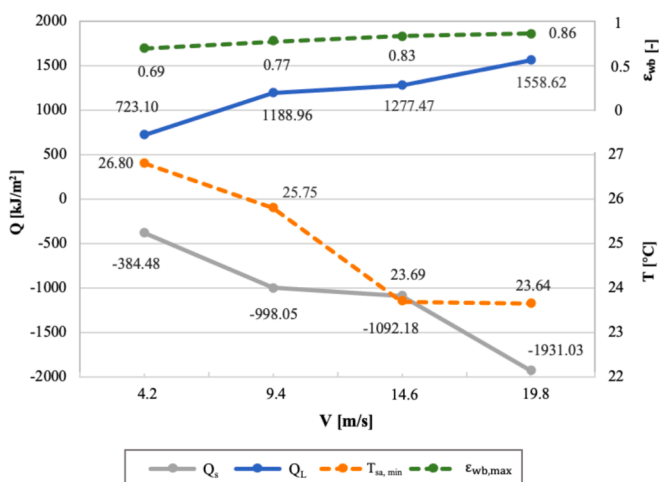


**Fig. 14.** Overlay sensible energy and latent energy, wet bulb effectiveness, minimum supply air temperature.

of a minimum achievable temperature limit. The wet bulb effectiveness followed a similar trend, being a maximum value of 0.86.

These results demonstrated the significant impact of manufacturing parameters on the behaviour of wet channels and highlighted the potential for incorporating these channels into direct or indirect evaporative cooling systems. Moreover, the versatility of Additive Manufacturing techniques provides a significant advantage for this purpose.

#### Declaration of competing interest

The authors declare that they have no known competing financial interests or personal relationships that could have appeared to influence the work reported in this paper.

#### Data availability

Data will be made available on request.

## Acknowledgement

These results are part of the project DCOOL, reference TED2021-129648B-I00, funded by MCIN/AEI/10.13039/501100011033 and the European Union “NextGeneration EU/PRTR”. Recovery, Transformation and Resilience Plan - funded by the European Union – NextGeneration EU. The authors also acknowledge the financial support received by European Union’s Horizon 2020 research and innovation programme, through the research project WEDISTRICT, reference H2020-WIDE-SPREAD2018-03-857801.

## References

- [1] International Energy Agency, The Future of Cooling Opportunities for energy-efficient air conditioning Together Secure Sustainable, 2018. [www.iea.org/t&c/](http://www.iea.org/t&c/).
- [2] International Energy Agency, World Energy Outlook 2023, 2023. [www.iea.org/terms](http://www.iea.org/terms).
- [3] IPCC, Cambio climático 2021 Bases físicas, 2021.
- [4] Y. Wang, X. Huang, L. Li, Comparative study of the cross-flow heat and mass exchangers for indirect evaporative cooling using numerical methods, *Energies* (Basel) 11 (2018), <https://doi.org/10.3390/en1123374>.
- [5] S.K. Gupta, B.B. Arora, A. Arora, Effect of evaporative cooling of condenser on the performance of air conditioner, *Iran. J. Sci. Technol. - Trans. Mech. Eng.* 47 (2023) 1661–1677, <https://doi.org/10.1007/s40997-023-00631-3>.
- [6] F. Comino, S. Milani, S. De Antonellis, C.M. Joppolo, M. Ruiz de Adana, Simplified performance correlation of an indirect evaporative cooling system: Development and validation, *Int. J. Refrig.* 88 (2018) 307–317, <https://doi.org/10.1016/j.ijrefrig.2018.02.002>.
- [7] M.W. Shahzad, J. Lin, B. Bin Xu, L. Dala, Q. Chen, M. Burhan, M. Sultan, W. Worek, K.C. Ng, A spatiotemporal indirect evaporative cooler enabled by transiently interceding water mist, *Energy* 217 (2021), <https://doi.org/10.1016/j.energy.2020.119352>.
- [8] X. Zhao, S. Liu, S.B. Riffat, Comparative study of heat and mass exchanging materials for indirect evaporative cooling systems, *Build. Environ.* 43 (2008) 1902–1911, <https://doi.org/10.1016/j.buildenv.2007.11.009>.
- [9] M.A. Arie, A.H. Shooshtari, R. Tiwari, S.V. Dessiatoun, M.M. Ohadi, J.M. Pearce, Experimental characterization of heat transfer in an additively manufactured polymer heat exchanger, *Appl. Therm. Eng.* 113 (2017) 575–584, <https://doi.org/10.1016/j.applthermaleng.2016.11.030>.
- [10] J. Castillo-González, F. Comino, F.J. Navas-Martos, M. Ruiz de Adana, Manufacturing and experimental analysis of a dew-point indirect evaporative cooler using fused deposition modelling 3D printing and polymeric materials, *Appl. Therm. Eng.* 230 (2023), <https://doi.org/10.1016/j.applthermaleng.2023.120683>.
- [11] R. Tiwari, R.S. Andhare, A. Shooshtari, M. Ohadi, Development of an additive manufacturing-enabled compact manifold microchannel heat exchanger, *Appl. Therm. Eng.* 147 (2019) 781–788, <https://doi.org/10.1016/j.applthermaleng.2018.10.122>.
- [12] O. Khalid, M. Ali, N.A. Sheikh, H.M. Ali, M. Shehryar, Experimental analysis of an improved Maisotsenko cycle design under low velocity conditions, *Appl. Therm. Eng.* 95 (2016) 288–295, <https://doi.org/10.1016/j.applthermaleng.2015.11.030>.
- [13] O. Khalid, Z. Butt, W. Tanveer, H.I. Rao, Design and experimental analysis of counter-flow heat and mass exchanger incorporating (M-cycle) for evaporative cooling, *Heat Mass Transf./Waerme- Und Stoffübertragung* 53 (2017) 1391–1403, <https://doi.org/10.1007/s00231-016-1914-2>.
- [14] J.K. Jain, D.A. Hindoliya, Experimental performance of new evaporative cooling pad materials, *Sustain Cities Soc.* 1 (2011) 252–256, <https://doi.org/10.1016/j.scs.2011.07.005>.
- [15] N.H. Kim, Performance of an indirect evaporative cooler (IEC) made of PET/cellulose composite sheet as wetting media, *Appl. Therm. Eng.* 186 (2021), <https://doi.org/10.1016/j.applthermaleng.2020.116492>.
- [16] Y. Gao, X. Song, D. Wei, P. Zhang, Performance evaluation of a porous polymer-nickel foam compound cooler combining radiative and evaporative cooling, *Sol. Energy* 264 (2023), <https://doi.org/10.1016/j.solener.2023.111983>.
- [17] W.J. Choi, K.S. Hwang, H.J. Kwon, C. Lee, C.H. Kim, T.H. Kim, S.W. Heo, J.H. Kim, J.Y. Lee, Rapid development of dual porous poly(lactic acid) foam using fused deposition modeling (FDM) 3D printing for medical scaffold application, *Mater. Sci. Eng. C* 110 (2020), <https://doi.org/10.1016/j.msec.2020.110693>.
- [18] C. T.Joen, Y. Park, Q. Wang, A. Sommers, X. Han, A. Jacobi, A review on polymer heat exchangers for HVAC&R applications, *Int. J. Refrig.* 32 (2009) 763–779, <https://doi.org/10.1016/j.ijrefrig.2008.11.008>.
- [19] S. Lowrey, C. Hughes, Z. Sun, Thermal-hydraulic performance investigation of an aluminium plate heat exchanger and a 3D-printed polymer plate heat exchanger, *Appl. Therm. Eng.* 194 (2021), <https://doi.org/10.1016/j.applthermaleng.2021.117060>.
- [20] A. Sapienza, V. Brancato, Y. Aristov, S. Vasta, Plastic heat exchangers for adsorption cooling: Thermodynamic and dynamic performance, *Appl. Therm. Eng.* 188 (2021), <https://doi.org/10.1016/j.applthermaleng.2021.116622>.
- [21] E. Velasco Gómez, A. Tejero González, F.J. Rey Martínez, Experimental characterisation of an indirect evaporative cooling prototype in two operating modes, *Appl. Energy* 97 (2012) 340–346, <https://doi.org/10.1016/j.apenergy.2011.12.065>.
- [22] Y. Wang, X. Huang, J. Chu, M. Qu, T. Li, C. Dai, Analysis of polishing waste ceramic foam packing in evaporative cooling, *Appl. Therm. Eng.* 212 (2022), <https://doi.org/10.1016/j.applthermaleng.2022.118477>.
- [23] E. Gkartzou, E.P. Koumoulos, C.A. Charitidis, Production and 3D printing processing of bio-based thermoplastic filament, *Manuf. Rev. (Les Ulis)* 4 (2017), <https://doi.org/10.1051/mfreview/2016020>.
- [24] M.J. Romero-Lara, F. Comino, M. Ruiz de Adana, Experimental assessment of the energy performance of a renewable air-cooling unit based on a dew-point indirect evaporative cooler and a desiccant wheel, *Energy Convers. Manag.* 310 (2024), <https://doi.org/10.1016/j.enconman.2024.118486>.
- [25] J. Wang, Q. Meng, L. Zhang, Y. Zhang, B.J. He, S. Zheng, M. Santamouris, Impacts of the water absorption capability on the evaporative cooling effect of pervious paving materials, *Build. Environ.* 151 (2019) 187–197, <https://doi.org/10.1016/j.buildenv.2019.01.033>.
- [26] L. Zhang, Z. Pan, Y. Zhang, Q. Meng, Impact of climatic factors on evaporative cooling of porous building materials, *Energy Build.* 173 (2018) 601–612, <https://doi.org/10.1016/j.enbuild.2018.05.038>.
- [27] S. Chakraborty, D. Vernon, A. Jha, V. Narayanan, Performance characterization of M-cycle indirect evaporative cooler and heat recovery ventilator for commercial buildings – Experiments and model, *Energy Build.* 281 (2023), <https://doi.org/10.1016/j.enbuild.2022.112762>.